An Accurate, Universal, and Fast Time Domain Model for Different Types of Resonant Converters by Considering Parasitic Capacitors and Deadtime

Ziang Li, *Student Member, IEEE*, Shuo Zhang, *Student Member, IEEE*, Dachuan Chen, Peng Sun, Yanjie He, *Student Member, IEEE*, Quanming Luo, *Member, IEEE*, Jinjun Liu, *Fellow, IEEE*, and Yuqi Wei, *Member, IEEE*

***Abstract*—The existing time domain models for *CLLLC* class resonant converters have at least one of the following drawbacks: 1) the model cannot be applied for different resonant tanks and circuit topologies; 2) the effect of parasitic capacitors and deadtime is ignored; 3) large computation time is required to obtain steady state waveforms. To address these issues, an advanced state-space based analysis (ASSA) model is proposed in this article. The operation stages by considering parasitic capacitors and deadtime are proposed and equivalent to a universal circuit, which largely increases the accuracy with low model complexity. Additionally, the ASSA model is universal for different inverter structures, rectifier structures, and different resonant tanks, including *LC, LLC, CLL, CLLC, and CLLLC*. To improve the calculation speed, a hybrid operation mode analysis and ASSA model is proposed to obtain closer initial values and achieve steady state 2.15 times faster than traditional state-space based analysis methods. Finally, experimental results of *CLLLC, CLLC*, and *LLC* resonant converters working in multiple conditions are presented to validate the effectiveness and accuracy of the proposed ASSA model. Compared with the traditional time domain model, the relative error of resonant inductor current waveforms is reduced from 5.91%–43.54% to 2.83%–19.42%.**

***Index Terms*—Deadtime, parasitic capacitor, resonant converter, time-domain model.**

Received 17 April 2024; revised 7 July 2024; accepted 29 July 2024. Date of publication 2 August 2024; date of current version 12 December 2024. This work was supported in part by the State Key Laboratory of Alternate Electrical Power System with Renewable Energy Sources under Grant LAPS23019, in part by the Opening Project of State Key Laboratory of Space-Power Sources, in part by the National Natural Science Foundation of China under Grant 52307221, and in part by the Aeronautical Science Fund under Grant ASFC-2022Z072070001. Recommended for publication by Associate Editor M. Monfared. *(Corresponding author: Yuqi Wei.)*

Ziang Li, Shuo Zhang, Yanjie He, Jinjun Liu, and Yuqi Wei are with the School of Electrical Engineering, Xi'an Jiaotong University, Xi'an 710049, China (e-mail: liziang463202@stu.xjtu.edu.cn; zsmailbox@stu.xjtu.edu.cn; jjliu@mail.xjtu.edu.cn; yuqiwei@xjtu.edu.cn).

Dachuan Chen is with the State Key Laboratory of Space Power-Sources, Shanghai Institute of Space Power-Sources, Shanghai 200245, China (e-mail: chendachuan@sjtu.edu.cn).

Peng Sun is with the School of State Key Laboratory of Alternate Electrical Power System with Renewable Energy Sources, North China Electric Power University, Beijing 100096, China (e-mail: sunpeng@ncepu.edu.cn).

Quanming Luo is with the School of Electrical Engineering, Chongqing University, Chongqing 400044, China (e-mail: lgm394@cqu.edu.cn).

Color versions of one or more figures in this article are available at https://doi.org/10.1109/TPEL.2024.3437251.

Digital Object Identifier 10.1109/TPEL.2024.3437251

I. Introduction

ISOLATED dc–dc converters are necessary in many industry applications, including microgrids, electric vehicles, and data center power supplies. Fig. 1 shows a typical structure of the hybrid microgrid, where the dc–dc converters play a key role. The voltage levels of the input side and the output side are always highly different. Therefore, isolated dc–dc converters are widely applied for the sake of voltage ratio requirement and the concern of safety. Among different isolated dc–dc converters, resonant converters have drawn much attention owning to their advantages of the wide soft-switching operation range and high efficiency operation characteristics [1].

However, the degraded efficiency performance for the wide voltage gain range, the complex design process for circuit parameters and magnetic components restricts the further popularization of the resonant converters [34], [35], [36].

Modeling of the resonant converters are of great importance to achieve the high-performance operation. Traditionally, the fundamental harmonic approximation (FHA) method is used to achieve the steady state characteristics analysis and the resonant converters design [2], [3], [4], [5], [6], [7], [8]. For FHA, only the fundamental harmonic of the circuit currents and voltages are considered, which leads to large errors especially when the converter's operating frequency is away from the resonant frequency. In order to reduce the large error of FHA model, extended harmonic approximation (EHA) models are proposed for *LLC* resonant converters by considering more harmonics [9], [10], which will increase the accuracy of FHA. However, the computation complexity is largely increased, and the overall analysis accuracy is still unsatisfactory for wide voltage range applications [11].

Therefore, the accurate time domain model is developed for resonant converters to obtain the steady state information and achieve optimal analysis and design. According to the different modeling approaches, the time domain modeling methods for resonant converters can be divided into two categories: operation mode analysis (OMA) [12], [13], [14], [15], [16], [17] and state-space based analysis (SSA) [16], [17]. OMA needs to analyze all the possible operation modes and establish their corresponding solvers, and can calculate the steady state waveforms with a fast speed. In [12], [13], [14], and [15], the operation modes of *LLC*

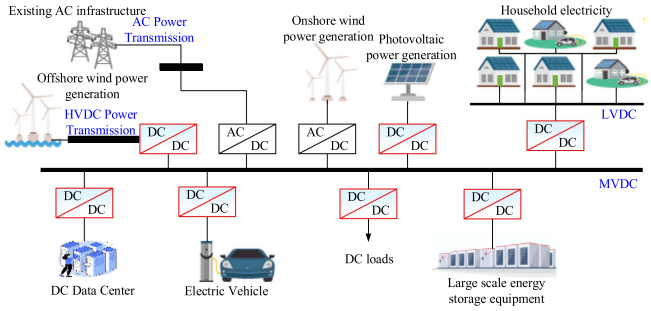

Fig. 1. Typical structure of hybrid microgrid.

resonant converter are discussed. The similar OMA analysis process for *CLL* resonant converter is discussed in [16] and [17]. Similarly, in [18], the OMA model for *CLLLC* resonant converter with symmetric resonant tank parameters (SCLLLC) is developed and the corresponding optimal design method is discussed. In [19], the effects of different inverter structures and rectifier structures are discussed and included into the OMA model of *LLC* resonant converters. To cover the different types of resonant tanks, different resonant tanks are equivalent to one universal circuit model based on the conversion of the lumped circuit in [20]. Nevertheless, the conversion process introduces extra complicated calculations.

Different from the complex OMA process and the steady state calculation of OMA, SSA only requires initial values of state variables and calculates the transient process from the initial values to steady state values. However, it needs much more calculation time to obtain steady state waveforms. The SSA analysis for the *CLLLC*-class isolated bidirectional dc–dc converter is developed in [21]. Additionally, it calculates the expressions based on *CLLLC* with asymmetric parameters (ACLLLC) and regards the other types of resonant tanks as special circumstances. Therefore, all types of resonant tanks can be easily covered. The SSA is further applied in the inductive power transfer system [22], the parameter design optimization stage of *CLLC* resonant converters [23], and the dynamic process analysis [24].

The results of OMA models and SSA models are both identical to the simulation results of ideal *CLLLC* resonant converters obtained by power simulation (PSIM), which are detailly shown in [18] and [21]. However, some technical issues emerge in the traditional time domain model by neglecting parasitic capacitors and deadtime. Yuan et al. [25] analyzed the effect of deadtime for *CLLLC* class resonant converters, especially when the deadtime effect is evident. The including of deadtime in the SSA can improve the modeling accuracy significantly, and takes more advantages in applications of parameter design, synchronous rectification (SR), zero voltage switching (ZVS) judgement and deadtime design. This model improves the accuracy, but cannot depict the high frequency resonance formed by the parasitic capacitors and the resonant inductors [26]. Ditze et al. [26] analyzed the effect of parasitic capacitors in resonant converters, including the high frequency oscillation phenomenon and the nonmonotonic gain curve phenomenon, which affect the application and control of resonant converters. Xiao et al. [27] considered the parasitic capacitors and deadtime for *LLC* resonant converter based on OMA model, and one accurate deadtime design strategy is proposed. However, this advanced OMA model has too many operation modes, which increases the modeling complexity significantly. Additionally, it only covers partial circumstances. In [28], an accurate SR strategy for *CLLLC* resonant converters is proposed by considering parasitic capacitors. However, the strategy is based on the symmetrical *CLLLC*. Additionally, the proposed time domain model in [27] and [28] did some approximations and was not accurate enough. In conclusion, an accurate, universal, and fast time-domain model by considering parasitic capacitors and deadtime with low complexity is not established.

These issues are improved significantly by the advanced SSA (ASSA) model proposed in this article. The contributions of this article are summarized as follows. For accuracy and simplicity, 1) by modifying traditional SSA model's operation stages, the effect of parasitic capacitors and deadtime is added, which highly improves the accuracy of traditional time domain model; 2) different working stages are equivalent to one universal circuit, which makes the universal expressions applicable for all operation stages and reduces the modeling complexity significantly. For rapidity, a hybrid OMA and SSA modeling method is proposed. The fast speed OMA model is applied to obtain the initial values, which is much closer to the steady state values compared with the traditional preset constant initial values. Therefore, the ASSA model can obtain steady-state waveforms much faster than the traditional SSA model. For universality, 1) by deriving the time-domain model for the most complicate ACLLLC circumstance, a universal model can be obtained for different resonant tanks, including *LC, LLC, CLL, CLLC, CLLLC* with symmetric parameters (SCLLLC) and ACLLLC; 2) the effects of different inverter structures and rectifier structures are discussed and included in the model. A comparison of the existing modeling methods for resonant converters are shown in Table I.

The rest of this article is organized as follows. The traditional time domain modeling methods for resonant converters are summarized and reviewed in Section II. The proposed ASSA model is introduced in Section III. The experimental results are presented and analyzed in Section IV to validate the proposed model. Finally, Section V concludes this article.

II. Review of the Time Domain Modeling Process for Resonant Converters

A. Assumptions, Operation Stages, Equivalent Circuits, and Time Domain Expressions

Considering the application requirement and based on the tradeoff of model accuracy and complexity, there are four assumptions for traditional time domain modeling process. These assumptions are reasonable in the converter-level model [11], [12], [13], [14], [15], [16], [17], [18], [19], [20].

1) The power conversion efficiency is assumed to be 100%.
2) The switching devices, magnetic components, resonant capacitors are regarded as ideal devices (the equivalent

TABLE I
COMPARISON OF DIFFERENT MODELING METHODS INTRODUCED IN EXISTING REFERENCES

Modeling method	Reference	Different resonant tanks	Different inverter and rectifier structures	Effect of parasitic capacitors	Effect of deadtime	Accuracy after considering non-ideal effects	Calculation speed	Model complexity after considering non-ideal effects
FHA	[2]-[8]	[7], [8]	Yes	[8]	No	⋆	⋆⋆⋆⋆	⋆
EHA	[9, 10]	Yes	Yes	[10]	No	⋆⋆	⋆⋆⋆	⋆⋆
OMA	[11]-[20], [26]-[28]	[20]	[19]	[27, 28]	[27]	⋆⋆⋆⋆	⋆⋆⋆	⋆⋆⋆⋆
SSA	[21]-[25]	[21, 23]	No	No	[25]	⋆⋆⋆	⋆	⋆⋆⋆
SSA	Proposed ASSA	Yes	Yes	Yes	Yes	⋆⋆⋆⋆⋆	⋆⋆	⋆⋆⋆

series resistors, parameters' variations under different ambient conditions and the parasitic capacitors are ignored).
3) The deadtime is ignored.
4) The modeling process for pulse frequency modulation (PFM) controlled resonant converter is selected as an example. The basic principle and modeling process for the other modulation strategies such as pulsewidth modulation are similar [21].

For different time domain modeling methods of resonant converters, the operation stages are established firstly to make the nonlinear system piecewise linear. The equivalent circuits, duration, and transition conditions of the different operation stages are introduced in this section.

Fig. 2(a) shows the topology of *CLLLC* class isolated dc–dc resonant converters, where $v_{\rm bp}(t)$ and $v_{\rm bs}(t)$ represent the output port voltage of primary side full bridge and secondary side full bridge. There are six operation stages for PFM controlled *CLLLC* class resonant converters. For the primary side, *CLLLC* works in I stage when $S_{1,\,4}$ turn ON and works in III stage when $S_{2,\,3}$ turn ON. For the secondary side, *CLLLC* works in P, N, O stages based on the conduction states of secondary side paralleled diodes [19]. When paralleled diodes of S_5, S_8 conduct, the secondary side bridge voltage $v_{\rm bs}/N$ is equal to $V_{\rm o}$ and *CLLLC* works in P stage. When paralleled diodes of S_6, S_7 conduct, $v_{\rm s}/N$ is equal to $-V_{\rm o}$ and *CLLLC* works in N stage. When paralleled diodes of S_{5-8} are OFF, *CLLLC* works in O stage. Based on different stages for primary side and secondary side, there are six stages in total ($P_{\rm I}$, $O_{\rm I}$, $N_{\rm I}$, $P_{\rm III}$, $O_{\rm III}$, $N_{\rm III}$). The equivalent circuits of all different stages converted to the primary side are shown in Fig. 2(b) and (c), where C_1 represents the primary side resonant capacitance value $C_{\rm r1}$, L_1 represents the primary side resonant inductance value $L_{\rm r1}$, $L_{\rm m}$ represents the magnetic inductance value, N represents the turns ratio, C_2 represents the converted secondary side resonant capacitance value $C_{\rm r2}/N^2$, and L_2 represents the converted secondary side resonant inductance value $N^2L_{\rm r2}$. The difference of I, III stages in the equivalent circuit is only the difference of $V_{\rm p}$.

The P, N stages' equivalent circuit, as shown in Fig. 2(b), is a fourth-order linear system. Since the different types of resonant tanks can be regarded as the special circumstances of *CLLLC* with asymmetric parameters (ACLLLC) [21], the time domain modeling process for ACLLLC is taken as an example. Time domain expressions for ACLLLC can be derived by Kirchhoff's law, as shown in (1)–(4) shown at the bottom of this page, where the resonant tank parameters $L_{\rm r1}$, $C_{\rm r1}$, $L_{\rm r2}$, $C_{\rm r2}$, and $L_{\rm m}$ can be any values. The waveforms of independent state variables $i_1(t)$, $i_2(t)$, $v_1(t)$, $v_2(t)$ at each moment can be calculated based on their initial values $i_1(0)$, $i_2(0)$, $v_1(0)$, $v_2(0)$ and the transfer matrix $T(t)$. The converter transfers into P stage only when $i_2 > 0$, and transfers into N stage only when $i_2 < 0$. In addition, P stage or N stage will be over when $i_2 = 0$ and $|v_m\text{-}v_2\text{-}v_{\rm L2}| < NV_{\rm O}$.

$$\begin{bmatrix} i_1(t) \\ i_2(t) \\ v_1(t)-V_{\rm p} \\ v_2(t)+V_{\rm s} \end{bmatrix} = T(t) \begin{bmatrix} i_1(0) \\ i_2(0) \\ v_1(0)-V_{\rm p} \\ v_2(0)+V_{\rm s} \end{bmatrix} = HS(t)\cdot ZH \cdot \begin{bmatrix} i_1(0) \\ i_2(0) \\ v_1(0)-V_{\rm p} \\ v_2(0)+V_{\rm s} \end{bmatrix} \tag{1}$$

$$HS(t) = \begin{bmatrix} C_1\cos(k_1t) & -C_1k_1\sin(k_1t) & C_1\cos(k_2t) & -C_1k_2\sin(k_2t) \\ C_2K_1\cos(k_1t) & -C_2k_1K_1\sin(k_1t) & C_2K_2\cos(k_2t) & -C_2k_2K_2\cos(k_2t) \\ \frac{1}{k_1}\sin(k_1t) & \cos(k_1t) & \frac{1}{k_2}\sin(k_2t) & \cos(k_2t) \\ \frac{K_1}{k_1}\sin(k_1t) & K_1\cos(k_1t) & \frac{K_2}{k_2}\sin(k_2t) & K_2\cos(k_2t) \end{bmatrix} \tag{2}$$

$$ZH = \begin{bmatrix} C_1 & 0 & C_1 & 0 \\ C_2K_1 & 0 & C_2K_2 & 0 \\ 0 & 1 & 0 & 1 \\ 0 & K_1 & 0 & K_2 \end{bmatrix}^{-1}, \quad \begin{cases} K_1 = \frac{k_1^2(L_1+L_{\rm m})-L_{\rm m}}{L_{\rm m}k_1^2} \\ K_2 = \frac{k_2^2(L_1+L_{\rm m})-L_{\rm m}}{L_{\rm m}k_2^2} \end{cases} \tag{3}$$

$$k_{1,,2} = \sqrt{\frac{(C_1L_1+C_1L_m+C_2L_2+C_2L_m) \pm \sqrt{(L_mC_2-L_mC_1+L_2C_2-L_1C_1)^2+4L_m^2C_1C_2}}{2C_1C_2(L_1L_2+L_1L_m+L_2L_m)}} \tag{4}$$

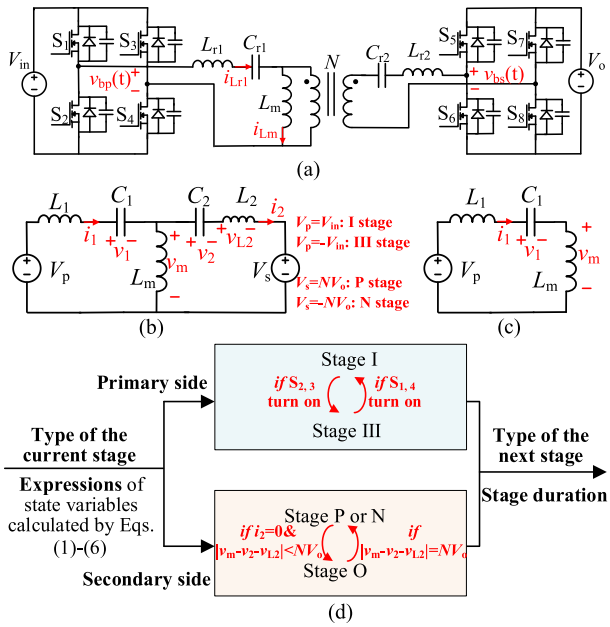

Fig. 2. Topology of *CLLLC* class isolated DC–DC resonant converters, different working stages' equivalent circuits and transition conditions. (a) Topology of *CLLLC*. (b) Equivalent circuit of P, N stages. (c) O stage. (d) Conditions for stages' transition.

The O stage's equivalent circuit shown in Fig. 2(c) is a second-order linear system. The time domain expressions can be derived as shown in (5) and (6). The transfer matrix of the O stage is $T_{\mathrm{O}}(t)$. The converter transfers into O stage only when $|v_m\text{-}v_2\text{-}v_{\mathrm{L2}}| < NV_{\mathrm{O}}$. The O stage will be over when $|v_m\text{-}v_2\text{-}v_{\mathrm{L2}}| = NV_{\mathrm{O}}$. The conditions for stages' transition are shown in Fig. 2(d), which are listed as follows:

1) $i_2 > 0 \rightarrow i_2(t) = 0$ and $|v_{\mathrm{m}}\text{-}v_2\text{-}v_{\mathrm{L2}}| < NV_{\mathrm{o}}$: P→O;
2) $i_2 < 0 \rightarrow i_2(t) = 0$ and $|v_{\mathrm{m}}\text{-}v_2\text{-}v_{\mathrm{L2}}| < NV_{\mathrm{o}}$: N→O;
3) $v_{\mathrm{m}}\text{-}v_2\text{-}v_{\mathrm{L2}} = NV_{\mathrm{o}}$: O→P;
4) $v_{\mathrm{m}}\text{-}v_2\text{-}v_{\mathrm{L2}} = \text{-}NV_{\mathrm{o}}$: O→N;
5) $S_{2,\,3}$ turn ON: I→III;
6) $S_{1,\,4}$ turn ON: III→I

$$\begin{bmatrix} i_1(t) \\ i_2(t) \\ v_1(t) - V_{\mathrm{p}} \\ v_2(t) + V_{\mathrm{s}} \end{bmatrix} = T_{\mathrm{O}}(t) \begin{bmatrix} i_1(0) \\ i_2(0) \\ v_1(0) - V_{\mathrm{p}} \\ v_2(0) + V_{\mathrm{s}} \end{bmatrix} \tag{5}$$

$$T_{\mathrm{O}}(t) = \begin{bmatrix} \cos(k_{\mathrm{O}}t) & 0 & -k_{\mathrm{O}}\sin(k_{\mathrm{O}}t) & 0 \\ 0 & 1 & 0 & 0 \\ \frac{1}{k_{\mathrm{O}}}\sin(k_{\mathrm{O}}t) & 0 & \cos(k_{\mathrm{O}}t) & 0 \\ 0 & 0 & 0 & 1 \end{bmatrix},$$

$$k_{\mathrm{O}} = \sqrt{\frac{1}{C_1(L_1 + L_m)}}. \tag{6}$$

B. OMA Time Domain Model

According to the process of traditional OMA model introduced in [11], [12], [13], [14], [15], [16], [17], [18], [19], and [20], there are three basic steps: 1) Calculate time domain expressions of three operation stages; 2) Establish solvers of different operation modes; 3) Judge the converter's operation mode and calculate the steady state waveforms based on the operation mode solvers in step 2. Step 1 is introduced in Section II-A. Steps 2 and 3 are introduced followingly.

1) Step 2: Establish Solvers for Different Operation Modes: OMA model only considers the steady state waveforms. When resonant converters work in steady state, the waveforms in the first half switching cycle are symmetric with the ones in the second half cycle, which means only the first half switching cycle needs to be considered. According to the occurrence order of the working stages in half switching cycle, resonant converters are divided into nine different operation modes shown in Table II [18], [19]. Take the PO mode as an example. Fig. 3 shows the typical waveform of the PO mode. During the first half switching cycle, the converter works in P stage at first, and enters O stage followingly. Therefore, time domain equations of the PO mode are established, as shown in (7)–(9), which are based on three categories of constrains: 1) symmetric - (7), which means the independent state variables' initial values and end values during the first half switching cycle should be opposite; 2) stage transition - (8), which means $i_2 = 0$ when P stage or N stage ends, $|v_m\text{-}v_2\text{-}v_{\mathrm{Lm}}| = NV_{\mathrm{O}}$ when O stage ends; 3) power conservation - (9), which means the system efficiency is assumed to be 100% and the input energy is equal to the output energy

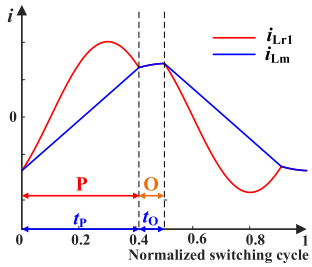

Fig. 3. Typical waveforms of inductors' current for PO mode.

$$\begin{bmatrix} -i_1(0) \\ -i_2(0) \\ -v_1(0) - V_{\mathrm{in}} \\ -v_2(0) + NV_{\mathrm{o}} \end{bmatrix} = \begin{bmatrix} i_1\left(\frac{T_{\mathrm{s}}}{2}\right) \\ i_2\left(\frac{T_{\mathrm{s}}}{2}\right) \\ v_1\left(\frac{T_{\mathrm{s}}}{2}\right) - V_{in} \\ v_2\left(\frac{T_{\mathrm{s}}}{2}\right) + NV_o \end{bmatrix}$$

$$= T_O\left(\frac{T_{\mathrm{s}}}{2} - t_{\mathrm{P}}\right) \cdot T(t_{\mathrm{P}}) \cdot \begin{bmatrix} i_1(0) \\ i_2(0) \\ v_1(0) - V_{\mathrm{in}} \\ v_2(0) + NV_{\mathrm{o}} \end{bmatrix} \tag{7}$$

$$i_2(t_{\mathrm{P}}) = 0 \tag{8}$$

$$\int_0^{t_{\mathrm{P}}} i_2(t) \cdot NV_{\mathrm{o}} dt = \frac{V_{\mathrm{o}}^2}{R_{\mathrm{L}}} \cdot \frac{T_{\mathrm{s}}}{2} \tag{9}$$

where $i_1(0)$, $i_2(0)$, $v_1(0)$, $v_2(0)$ are the initial values, $i_1(T_{\mathrm{s}}/2)$, $i_2(T_{\mathrm{s}}/2)$, $v_1(T_{\mathrm{s}}/2)$, $v_2(T_{\mathrm{s}}/2)$ are the end values during the first half switching cycle, T_{s} is the switching cycle, t_{P} is the duration of P stage, and R_{L} is the load resistance.

TABLE II
OPERATION MODES FOR RESONANT CONVERTERS

Switching frequency	$f_s<f_r$ Low → High					$f_s=f_r$	$f_s>f_r$ Low → High				
Operation mode	PN	PON	PO	OPO	O	P	O	NP	NOP	OP	OPO
Typical waveforms	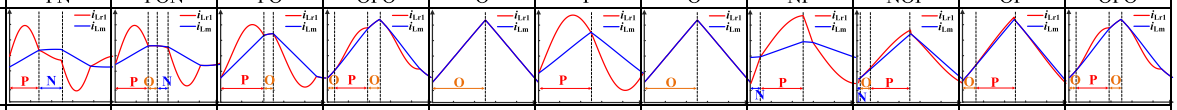										
Voltage gain	Buck/Boost	Buck/Boost	Boost	Boost	Boost	Unity	Buck	Buck	Buck	Buck	Buck
Output load	Heavy → Light				No load	Independent of load	No load	Heavy → Light			

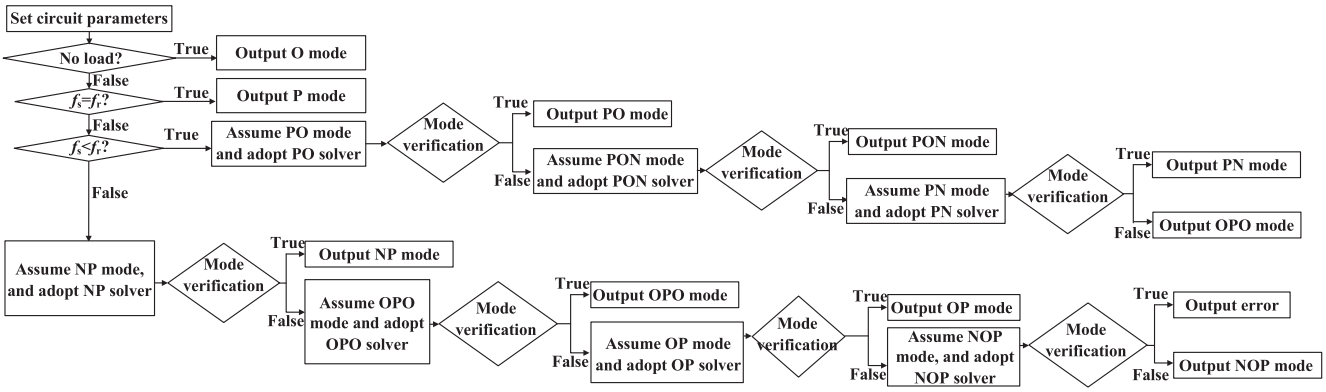

Fig. 4. Flowchart of assumption and verification method for open-loop operation mode judgement.

The OMA differs for open-loop operation and the closed-loop operation (PFM controlled) [19]. For open-loop calculation, assume $i_1(0)$, $i_2(0)$, $v_1(0)$, $v_2(0)$, t_P, V_o as six unknown parameters, which can be solved by six independent equations shown in (7)–(9). Similarly, for closed-loop calculation, $i_1(0)$, $i_2(0)$, $v_1(0)$, $v_2(0)$, t_P, T_s can be assumed as six unknown parameters and solved by (7)–(9). These linear differentiable equations can be regarded as the PO solver and solved by numerical-based computation tool (MATLAB is selected in this article). For the other operation modes' solvers, the equations can all be established similarly based on the same constraints of symmetric, stage transition and power conservation, which are not described in detail.

2) Step 3: Operation Mode Judgement: Before adopting the mode solvers established above, the converter's operation mode should be judged. The existing operation mode judgement methods can be divided into two categories: 1) assumption and verification method [19]; 2) operation mode boundary calculation method [20].

For assumption and verification methods, the operation mode is assumed at first, and then verified based on the conditions for stages' transitions shown in Fig. 2(d). Take the PO mode as an example, the converter's current waveforms $i_1(t)$, $i_2(t)$ and voltage waveforms $v_1(t)$, $v_2(t)$ can be obtained based on PO solver established in Section II-B. The PO mode judgement can be realized if $i_2(\Delta) > 0$ during P stage, and $|v_m\text{-}v_2\text{-}v_{L2}| < NV_O$ during O stage, where Δ is a very short time interval. In addition, it can be concluded from Table II that PN, PON, PO, OPO modes exist when $f_s < f_r$, NP, NOP, OP, OPO modes exist when $f_s > f_r$, P mode exists when $f_s = f_r$, O mode exists only when there is no load. Therefore, according to the different switching frequencies and load circumstances, the assumption and verification process for open-loop conditions can be conducted, as shown in Fig. 4. The process for closed-loop conditions is similar, which is not described in this article.

For operation mode boundary calculation methods, the operation modes' boundaries can be calculated by additional equations established based on the boundary constraint. Take the boundary of PO/PON modes as an example, the converter enters N stage at the end of the first half switching cycle ($t = T_s$), and the duration time of N stage can be regarded as zero. Therefore, an additional equation (10) based on the boundary constraint can be added into PO solver, and an additional unknown parameter R_L can be added. By solving the new PO solver, the boundary load resistance R_{LB} can be solved, and the judgement of PO/PON modes can be conducted based on the comparison of the realistic load resistance value R_L and R_{LB}. The other boundaries can be solved similarly

$$v_m(T_s) - v_2(T_s) - v_{L2}(T_s) = -NV_o. \tag{10}$$

C. State-Space Based Time Domain (SSA) Model

According to the process of SSA models introduced in [21], [22], [23], [24], and [25], there are four basic steps.

1) Get the initial values of independent state variables (i_1, i_2, v_1, v_2) and the initial stage of the resonant converter. Since the SSA method is not sensitive to the initial values of independent state variables, their initial values are directly set as zero or preset constant values obtained by estimation or simulation.

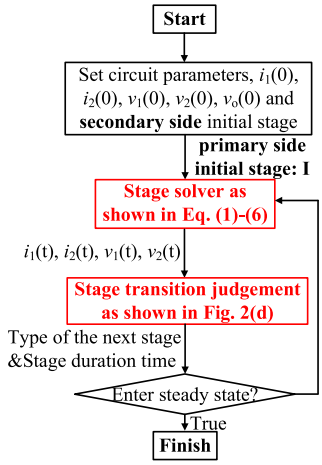

Fig. 5. Flowchart of the SSA model.

2) Calculate the values of i_1, i_2, v_1, v_2 during each stage based on the transfer matrix shown in (1)–(6).
3) Calculate the duration of the current operation stage based on the transition conditions, as shown in Fig. 2(d).
4) Circulate step 2, 3 and stop only when state variables approximately equal to the previous switching cycle, which means the resonant converter enters the steady state. The flowchart of the SSA calculation process is shown in Fig. 5.

The transfer matrixes shown in (1)–(4) illustrate that the characteristic roots of P, N stages are two sets of imaginary roots. Therefore, the waveforms of i_1, i_2, v_1, v_2 during P, N stages are the combination of two sinusoidal components. Their angular frequencies are k_1 and k_2. Similarly, the characteristic roots of the O stage are one set of imaginary roots, which means the waveforms of i_1, v_1 during O stage are sinusoidal values of one angular frequency k_O, while the values of i_2, v_2 during O stage are constant values. Additionally, the angular frequency k_1 is the resonant angular frequency ω_r of the resonant converter. Equation (11) shown at the bottom of this page, shows the expression

The results of OMA models and SSA models are both identical to the simulation results of ideal *CLLLC* resonant converters obtained by PSIM, which are detailly shown in [18] and [21]. OMA model only cares about the steady state waveforms, and the process of solving linear differentiable equations is not complex. There are many fast-speed packaged functions in MATLAB for solving linear equations such as *fsolve*. The SSA model can get the dynamic process of resonant converters from initial values to steady state values. However, this process always needs thousands of switching cycles' calculation, which will make the process of obtaining steady state waveforms much longer than the OMA model. To verify the calculation speed, after establishing the OMA model and the SSA model

TABLE III
COMPARISON OF AVERAGE CALCULATION TIME

Working Conditions (1000 random parameters are selected)	Average calculation time/ms		
L_{r1}, L_{r2}, L_m: 10~100 uH; R_L: 30~150 Ω;	OMA-1	OMA-2	SSA
C_{r1}, C_{r2}: 50~150 nF; f_s: 50~150 kHz	5.342	5.672	471.3

in MATLAB, the waveforms of the same 1000 random working conditions [including different resonant tank parameters, load resistors (R_L), and switching frequencies (f_s)] are calculated. A comparison of average calculation time for OMA and SSA models are shown in Table III. According to the different operation mode judgement methods introduced in Section II-B, OMA is divided into two types. OMA-1 means the assumption and verification method is applied; OMA-2 means the operation mode boundary calculation method is applied. These two operation mode judgement methods have similar calculation speed.

III. PROPOSED ACCURATE, UNIVERSAL, AND FAST TIME DOMAIN MODEL BY CONSIDERING PARASITIC CAPACITORS AND DEADTIME

A. Assumptions, Proposed Operation Stages and Their Universal Equivalent Circuits

Compared with the traditional models' assumptions, there are three main differences in the proposed model, which can reduce the idealization degree and improve the modeling accuracy.

1) The parasitic capacitors of switching devices are included. Their values are obtained based on the equivalent linear process introduced in [29], which is widely applied in the converter-level circuit models [27], [28], [30], [31].
2) The transformer's parasitic capacitor (C_T) can be included in resonant tanks including *LC, LLC, CLL, CLLC*. For *CLLLC* resonant converters, it can be included only when the resonant inductors are integrated into the transformer. The reason and the process of considering C_T are discussed in Section III-D. C_T is ignored before Section III-D.
3) The deadtime is included and its value has no limitation.

To clearly show the modeling process, the first half switching cycle is taken as an example since it has same operation stages with the second half switching cycle. Fig. 6 shows the nine operation stages by taking parasitic capacitors and deadtime into consideration.

The secondary side can be divided into P, O, N stages, representing three situations: 1) paralleled diodes of S_5, S_8 conduct, $v_{bs}(t) = V_o$; 2) Secondary side switches' parasitic capacitors C_{oss2} charging and discharging process, $v_{bs}(t)$ is time-varying; 3) paralleled diodes of S_6, S_7 conduct, $v_{bs}(t) = -V_o$. Their equivalent circuits are depicted in Fig. 6(b). The equivalent process for stages P, N is simple by neglecting the

$$\begin{cases} \omega_r = \sqrt{\dfrac{(C_1L_1+C_1L_m+C_2L_2+C_2L_m)+\sqrt{(L_mC_2-L_mC_1+L_2C_2-L_1C_1)^2+4L_m^2C_1C_2}}{2C_1C_2(L_1L_2+L_1L_m+L_2L_m)}} \\ f_r = \dfrac{\omega_r}{2\pi} \end{cases}. \tag{11}$$

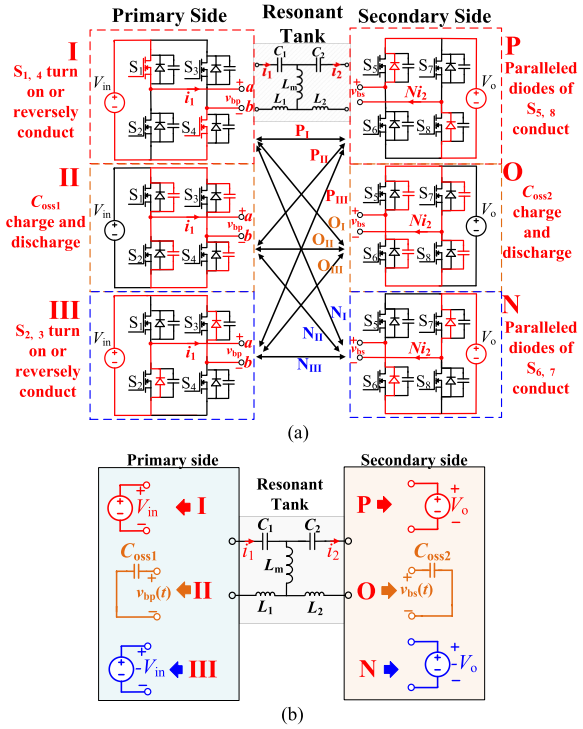

Fig. 6. Nine operation stages by considering parasitic capacitors and deadtime and their equivalent circuits. (a) Nine operation stages. (b) Equivalent circuits of the nine operation stages.

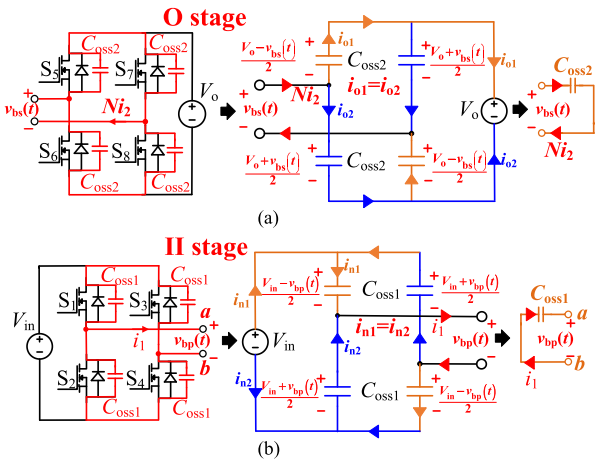

Fig. 7. Equivalent process of O stage and II stage. (a) Equivalent process of O stage. (b) Equivalent process of II stage.

ON-state resistance of switches. However, during O stage, the process is different, which is shown in Fig. 7(a). For traditional O stage, the secondary side current Ni_2 is regarded as zero, which means only the primary side's circuit elements are considered. By considering parasitic capacitors, O stage can be regarded as the charging and discharging stage of C_{oss2}. Therefore, the secondary side current Ni_2 is not zero and $v_{bs}(t)$ is time-varying, which means the secondary side's circuit elements should be considered. In addition, the current of secondary side bridge i_{o1} and i_{o2} shown in Fig. 7 are identical. Therefore, the parasitic capacitors are paralleled and can be equivalent to one capacitor

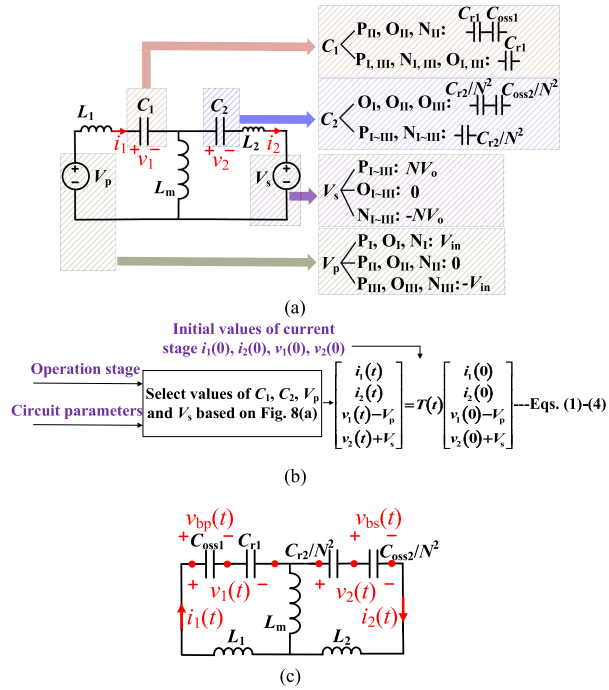

Fig. 8. Universal equivalent circuit and state variables' solver of nine operation stages. (a) Universal equivalent circuit. (b) Stage solver for nine different stages. (c) Equivalent circuit of the stage O_{II}.

C_{oss2}. The initial voltage value of C_{oss2} during each stage is defined as $v_{bs}(0)$. The charging period of C_{oss2} is over when $v_{bs}(t) = V_o$ (enters P stage) or $v_{bs}(t) = -V_o$ (enters N stage).

The primary side can be divided into I, II, III stages, representing three situations: 1) $S_{1,4}$ turn ON or reversely conduct, $v_{bp}(t) = V_{in}$; 2) Primary side switches' parasitic capacitors C_{oss1} charging and discharging process, $v_{bp}(t)$ is time varying; 3) $S_{2,3}$ turn ON or reversely conduct, $v_{bp}(t) = -V_{in}$. Stage II only happens during the deadtime. Their equivalent circuits are also depicted in Fig. 6(b). The equivalent process for stage I, III is simple by neglecting the on-state resistance of switches. The equivalent process for stage II, as shown in Fig. 7(b), is similar as the process for O stage.

There are nine stages (P_I, O_I, N_I, P_{II}, O_{II}, N_{II}, P_{III}, O_{III}, N_{III}) by combining the primary and secondary sides. Their equivalent circuits are depicted in Fig. 6(b) and they have high similarity. Therefore, these nine stages can be equivalent to one universal circuit with different parameters, as shown in Fig. 8, where L_1 is equal to L_{r1}, L_2 is equal to N^2L_{r2}. L_1, L_2, C_1, and C_2 are four independent storage elements (L_m is not independent). Therefore, the equivalent circuit can be regarded as a fourth-order system, the independent state variables are i_1 (current of L_1), i_2 (current of L_2), v_1 (voltage of C_1), and v_2 (voltage of C_2).

For the primary side, when the resonant converter operates at I, III stages, the primary side's equivalent circuit is a dc voltage source with values of V_{in} or $-V_{in}$. Therefore, during I, III stages, C_1 is equal to C_{r1}, V_p is equal to V_{in} or $-V_{in}$. When resonant converter operates at II stage, the primary side's equivalent circuit is the capacitor C_{oss1}, as shown in Fig. 7(b).

Therefore, during II stage, C_1 is equal to C_{r1} in series with C_{oss1}, and V_p is equal to zero.

Similarly, for the secondary side, when the resonant converter operates at P, N stages, the secondary side's equivalent circuit is a dc voltage source with values of V_o or $-V_o$. Therefore, during P, N stages, after converted to the primary side, C_2 is equal to C_{r2}/N^2, and V_s is equal to NV_o or $-NV_o$. When resonant converter operates at O stage, the secondary side's equivalent circuit is the capacitor C_{oss2}, as shown in Fig. 7(a). Therefore, during O stage, after converted to the primary side, C_2 is equal to C_{r2}/N^2 in series with C_{oss2}/N^2, and V_s is equal to zero. The expressions of $v_{bp}(t)$ during stage II and $v_{bs}(t)$ during stage O are shown in (12). $v_{bp}(0)$, $v_1(0)$, $v_{bs}(0)$, and $v_2(0)$ are the initial values of $v_{bp}(t)$, $v_1(t)$, $v_{bs}(t)$, and $v_2(t)$ during each stage. Equation (12) can be derived based the equivalent circuit of O_{II} stage shown in Fig. 8(c).

In conclusion, when resonant converter operates at different stages, the topology of the equivalent circuits is universal. The only difference is the values of V_p, V_s, C_1, and C_2. Their values of different stages are shown in Fig. 8(a). Therefore, the waveforms during each stage can all be derived based on same expressions by simply replacing the values of V_p, V_s, C_1, and C_2 of (1)–(4). The solver for state variables' waveforms is shown in Fig. 8(b), where $i_1(0)$, $i_2(0)$ are the initial values of $i_1(t)$, $i_2(t)$ during each stage

$$\begin{cases} v_{bp}(t) = \frac{(v_1(t)-v_1(0))\cdot C_{r1}}{C_{r1}+C_{oss1}} + v_{bp}(0) \\ v_{bs}(t) = \frac{(v_2(t)-v_2(0))\cdot C_{r2}}{C_{r2}+C_{oss2}} + v_{bs}(0). \end{cases} \tag{12}$$

B. Characteristics of OMA and SSA

After deriving the nine stages by considering parasitic capacitors and deadtime, the following modeling process can be either OMA or SSA. Therefore, this section illustrate the characteristics of two modeling methods and the necessity of adopting SSA modeling process.

OMA is often applied in time domain analysis for resonant converters. OMA can be easily applied by establishing nine solvers since there are only three stages (P, O, N) and nine possible modes (P, PO, PON, PN, OPO, NP, NOP, OP, O) when neglecting parasitic capacitors and deadtime. However, after considering the nonideal effects, the stages' types are increased from 6 to 9, and the operation modes' number increases significantly. Fig. 9 shows two typical normalized waveforms of v_{bp} and v_{bs} obtained by PSIM. Many stages' transitions occur in the first half switching cycle. The transition situations vary significantly when working conditions or circuit parameters change.

This phenomenon can be explained as follows. During the O stage, C_{oss2} and the resonant tank parameters (C_{r1}, C_{r2}, L_{r1}, L_{r2}) form a new resonant frequency $f_{r,\,oss2}$. The expression of $f_{r,\,oss2}$ is shown in (13) shown at the bottom of the next page. C_{oss2} is often much smaller than resonant capacitors C_{r1}, C_{r2}. Therefore, $f_{r,\,oss2}$ is much higher than f_r, which means a high frequency oscillation process occurs during the O stage. However, the value of $f_{r,\,oss2}$ differs significantly with the varying of C_{oss2} values and load resistance. The number of high frequency resonant

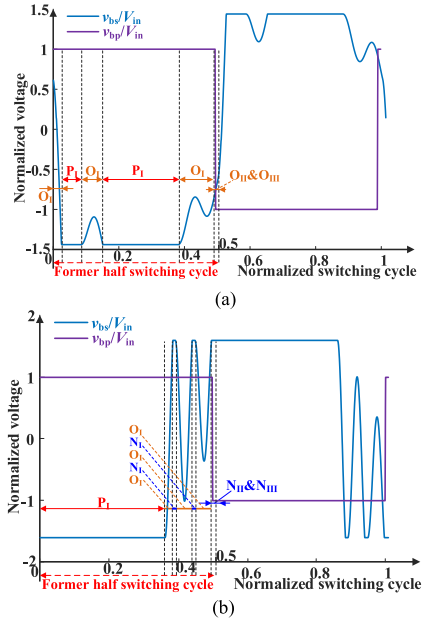

Fig. 9. Two typical circumstances of resonant converters obtained by PSIM simulation results when $L_{r1} = 94.8\ \mu$H, $L_{r2} = 64.3\ \mu$H, $L_m = 208\ \mu$H, $C_{r1} = 58.6$ nF, $C_{r2} = 53$ nF, $N = 13{:}15$, $C_{oss1} = 300$ pF, deadtime $= 180$ ns, $V_{in} = 100$ V. (a) $f_s = 55$ kHz, $R_L = 3000\ \Omega$, $C_{oss2} = 400$ pF. (b) $f_s = 53.5$ kHz, $R_L = 160\ \Omega$, $C_{oss2} = 180$ pF.

cycle during the former half switching cycle may change a lot for different working conditions, which can be shown in Fig. 9. Additionally, the N stage only occurs for partial situations, and these situations are hard to be predicted or summarized. The excessive possibilities and their irregularity make the OMA can only be implemented with approximated and simplified results [27], which will result in the loss of precise and universality

However, the increasing modes' possibilities have few effects on SSA modeling process. SSA model focus on the duration and transition conditions of working stages. Though the number of stages' type is increased from 6 to 9, the transition conditions of the proposed stages are clear and simple, as shown in Fig. 10. Therefore, the SSA modeling process can be easily adopted in the proposed model. The stages' transition conditions are listed as follows:

1) $i_2(t) > 0 \rightarrow i_2(t) < 0$: P→O;
2) $i_2(t) < 0 \rightarrow i_2(t) > 0$: N→O;
3) $v_{bs}(t) = V_o$: O→P;
4) $v_{bs}(t) = -V_o$: O→N;
5) during deadtime and $i_1(t) < 0$: III→II;
6) during deadtime and $i_1(t) > 0$: I→II;
7) $v_{bp}(t) = V_{in}$: II→I;
8) $v_{bp}(t) = -V_{in}$: II→III.

C. Distribution of Stages and the Flowchart of the Proposed Method

Fig. 11(a) shows the typical waveforms of *CLLLC* resonant converter when $f_s < f_r$ (PO mode in OMA model is chosen as an example) and the distribution of different stages, where T_{sn} means the normalized switching cycle. During the first half

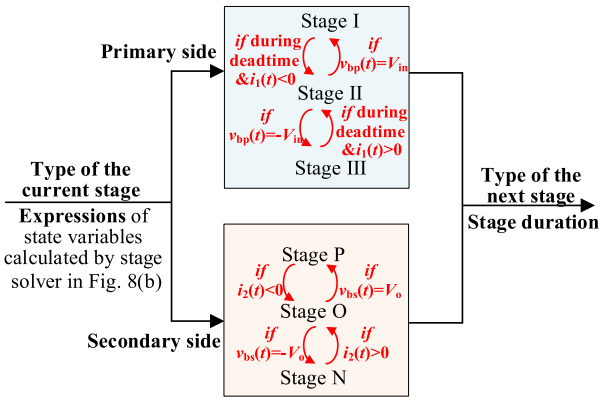

Fig. 10. Transition conditions for the proposed stages.

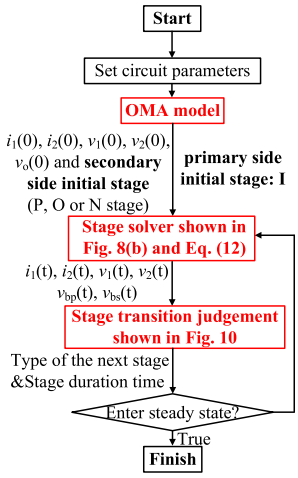

Fig. 12. Flowchart of the proposed ASSA model.

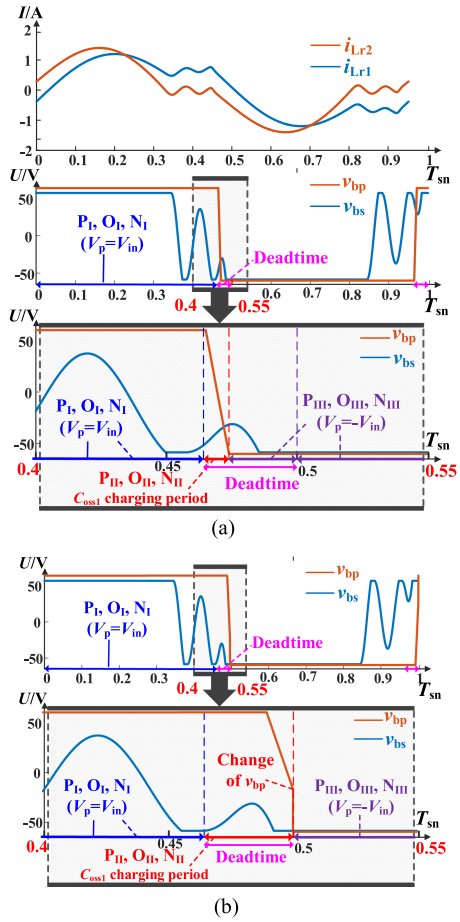

Fig. 11. Typical waveforms and stages' distribution of ASSA model. (a) ZVS is achieved, $S_{2,\,3}$ turn ON during stage III. (b) ZVS is not achieved, $S_{2,\,3}$ turn ON during stage II.

cycle ($T_{sn} \leq 0.5$), the stages distribution will be: P_I, O_I, N_I ($S_{1,\,4}$ turn ON)→P_{II}, O_{II}, N_{II} (C_{oss1} charge and discharge during deadtime)→ P_{III}, O_{III}, N_{III} ($S_{2,\,3}$ reversely conduct during deadtime), while the second half cycle ($0.5 < T_{sn} < 1$) will be P_{III}, O_{III}, N_{III} ($S_{2,\,3}$ turn ON)→P_{II}, O_{II}, N_{II} (C_{oss1} charge and discharge during deadtime)→ P_I, O_I, N_I ($S_{2,\,3}$ reversely conduct during deadtime). The distribution of stages for other operation modes are identical to PO mode.

By integrating the duration and transition conditions of different stages, the flowchart of proposed ASSA model is shown in Fig. 12. A step-by-step introduction is listed as follows.

1) After setting the circuit parameters, the initial values are calculated based on the traditional OMA model. Compared with the zero initial values or preset constant initial values applied in [21], [22], [23], [24], and [25], the initial values obtained by OMA model can be much closer to the steady state values. Therefore, ASSA model can have a faster calculation speed, which is detailly illustrated in Section IV-B
2) After the initial values and current stage is determined, the state variables' values during each stage can be obtained based on the stage solver, as shown in Fig. 8(b). The stage solver can adopt universal equations for all stages, which reduce the model's complexity significantly.
3) According to the calculated state variables' values, judge the duration time of current stage and the type of next stage using the stage transition conditions in Fig. 10.
4) When the state variables are approximately identical to the former switching cycle, the circuit can be regarded as entering the steady state, and the calculation will finish.

Additionally, the former modeling process assumes the realization of ZVS. When ZVS is not achieved, the stages distribution during the first half cycle will be: P_I, O_I, N_I ($S_{1,\,4}$

$$\begin{cases} f_{r,oss2} = \sqrt{\dfrac{(C_1L_1+C_1L_m+C_2L_2+C_2L_m)+\sqrt{(L_mC_2-L_mC_1+L_2C_2-L_1C_1)^2+4L_m^2C_1C_2}}{8\pi^2C_1C_2(L_1L_2+L_1L_m+L_2L_m)}} \\ C_1 = C_{r1}, C_2 = \dfrac{\frac{C_{r2}}{N^2}C_{oss2}}{C_{oss2}+\frac{C_{r2}}{N^2}}, L_1 = L_{r1}, L_2 = L_{r2}. \end{cases} \tag{13}$$

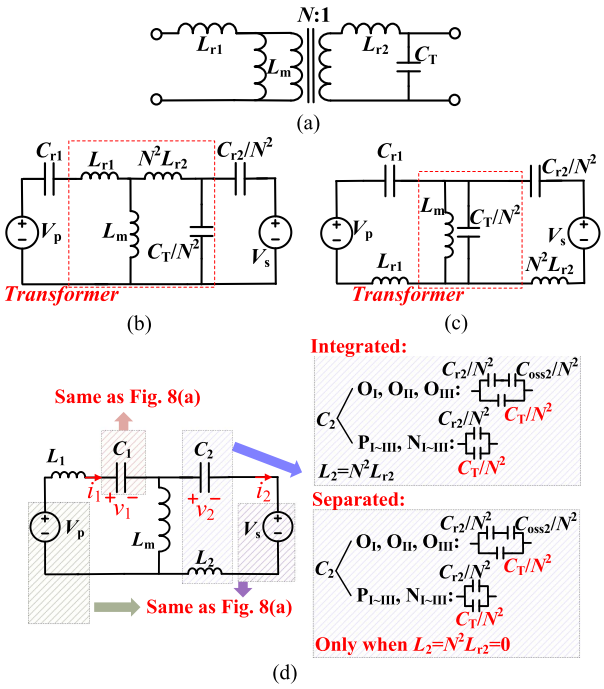

Fig. 13. Equivalent circuits of the transformer, resonant converters when considering transformer's parasitic capacitor (C_T). (a) One-order lumped stray capacitance model. (b) Resonant inductors are integrated. (c) Resonant inductors are separated. (d) Equivalent circuit when considering C_T.

turn ON)→P_{II}, O_{II}, N_{II} (C_{oss1} charge and discharge during deadtime), while the second half cycle will be P_{III}, O_{III}, N_{III} ($S_{2,\ 3}$ turn ON)→P_{II}, O_{II}, N_{II} (C_{oss1} charge and discharge during deadtime). The waveforms when ZVS is achieved or not achieved are compared in Fig. 11. The modeling process for these two conditions are identical, which can both be covered by Figs. 10 and 12.

D. Considering of the Transformer's Parasitic Capacitor

The modeling process introduced earlier has ignored the transformer's parasitic capacitor (C_T). The one-order lumped stray capacitance model introduced in [32] is adopted in the following process, which is shown in Fig. 13(a).

When resonant inductors are integrated into the transformer, the leakage inductances L_{r1} and L_{r2} in Fig. 13(a) are applied as resonant inductors. The equivalent circuit is shown in Fig. 13(b). The including of C_T will not increase the order of the equivalent circuit. The only difference is the values of C_2, which is shown in Fig. 13(d).

When resonant inductors are separated, L_{r1} and L_{r2} in Fig. 13(a) are regarded as zero. The considering of C_T has no influence on the equivalent circuit only when $L_{r2} = 0$ (when resonant tanks are *LC, LLC, CLL, CLLC*), and the only difference is the values of C_2, which is shown in Fig. 13(d). However, when L_{r2} is not zero (*CLLLC* resonant tank), the equivalent circuit will be a fifth-order system. The expressions will be much more complex, which is not included in the proposed ASSA model.

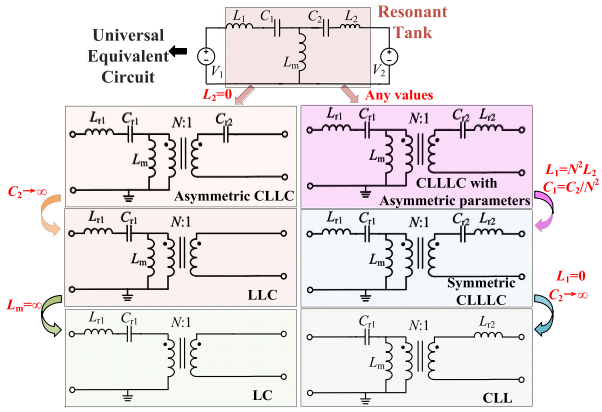

Fig. 14. Promotion to different resonant tanks.

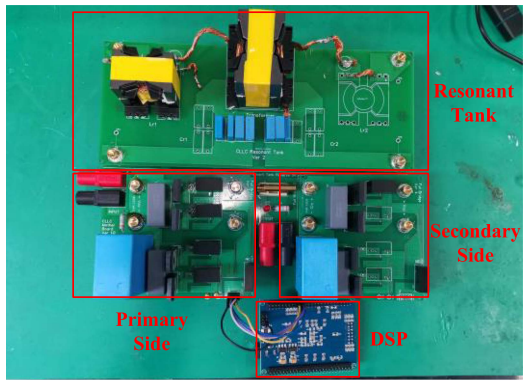

Fig. 15. Experimental platform.

In conclusion, when considering C_T, the flowchart of Fig. 12 can be applied for *LC, LLC, CLL, CLLC*. For *CLLLC* resonant converters, it can be applied only when the resonant inductors are integrated into the transformer. The C_2's values can be adjusted according to Fig. 13(d).

E. Extension to Different Resonant Tanks, Power Transmission Directions, and Structures of the Inverter and Rectifier

1) Different Types of Resonant Tanks: The six types of widely used resonant tanks are shown in Fig. 14 . Since the universal equivalent circuit is derived based on the most complicate situation of *CLLLC* with asymmetric resonant tank parameters, the other types of resonant tanks can be regarded as the special circumstances: 1) Symmetric *CLLLC*: $L_1 = N^2L_2$, $C_1 = C_2/N^2$; 2) Asymmetric *CLLC*: $L_2 = 0$; 3) *LLC*: $L_2 = 0$, $C_2 \to \infty$; 3) *CLL*: $L_1 = 0$, $C_2 \to \infty$; 4) *LC*: $L_2 = 0$, $C_2 \to \infty$, $L_m \to \infty$.

Additionally, the inductance values L_1, L_2 are not in the denominator as a product term. Therefore, L_1 and L_2 can be directly set as zero during the ASSA calculation process. When $C_1 \to \infty$ or $C_2 \to \infty$ is needed, values of C_1, C_2 can be enlarged greatly compared with the common values of resonant capacitors. For example, if the commonly used values for resonant capacitors are nF level, the values of C_1, C_2 can be set as μF or mF level when $C_1 \to \infty$ or $C_2 \to \infty$ is needed.

TABLE IV
DIFFERENT STRUCTURES OF INVERTERS AND RECTIFIERS

	Full-bridge inverter: 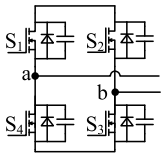	Symmetric half-bridge inverter 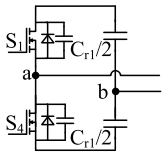	Asymmetric half-bridge inverter 
Full-bridge rectifier 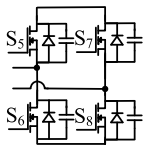	No modification	$\boldsymbol{C_{oss1}=2C_{oss1}}$ $V_s\begin{cases}P_{I\sim III}:NV_o\\O_{I\sim III}:Nv_{bs}(0)\\N_{I\sim III}:-NV_o\end{cases},V_p\begin{cases}P_I,O_I,N_I:V_{in}/2\\P_{II},O_{II},N_{II}:v_{bp}(0)\\P_{III},O_{III},N_{III}:-V_{in}/2\end{cases}$	$\boldsymbol{C_{oss1}=2C_{oss1}}$ $V_s\begin{cases}P_{I\sim III}:NV_o\\O_{I\sim III}:Nv_{bs}(0)\\N_{I\sim III}:-NV_o\end{cases},V_p\begin{cases}P_I,O_I,N_I:V_{in}\\P_{II},O_{II},N_{II}:v_{bp}(0)\\P_{III},O_{III},N_{III}:0\end{cases}$
Center-tapped transformer 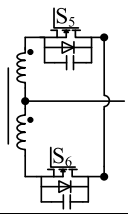	$\boldsymbol{C_{oss2}=2C_{oss2}}$	$\boldsymbol{C_{oss2}=2C_{oss2}}$, $\boldsymbol{C_{oss1}=2C_{oss1}}$ $V_s\begin{cases}P_{I\sim III}:NV_o\\O_{I\sim III}:Nv_{bs}(0)\\N_{I\sim III}:-NV_o\end{cases},V_p\begin{cases}P_I,O_I,N_I:V_{in}/2\\P_{II},O_{II},N_{II}:v_{bp}(0)\\P_{III},O_{III},N_{III}:-V_{in}/2\end{cases}$	$\boldsymbol{C_{oss2}=2C_{oss2}}$, $\boldsymbol{C_{oss1}=2C_{oss1}}$ $V_s\begin{cases}P_{I\sim III}:NV_o\\O_{I\sim III}:Nv_{bs}(0)\\N_{I\sim III}:-NV_o\end{cases},V_p\begin{cases}P_I,O_I,N_I:V_{in}\\P_{II},O_{II},N_{II}:v_{bp}(0)\\P_{III},O_{III},N_{III}:0\end{cases}$
Voltage doubler rectifier 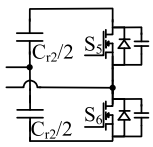	$\boldsymbol{C_{oss2}=2C_{oss2}}$, $\boldsymbol{R_L=4R_L}$ $V_s\begin{cases}P_{I\sim III}:NV_o/2\\O_{I\sim III}:Nv_{bs}(0)\\N_{I\sim III}:-NV_o/2\end{cases}$	$\boldsymbol{C_{oss2}=2C_{oss2}}$, $\boldsymbol{R_L=4R_L}$, $\boldsymbol{C_{oss1}=2C_{oss1}}$ $V_s\begin{cases}P_{I\sim III}:NV_o/2\\O_{I\sim III}:Nv_{bs}(0)\\N_{I\sim III}:-NV_o/2\end{cases},V_p\begin{cases}P_I,O_I,N_I:V_{in}/2\\P_{II},O_{II},N_{II}:v_{bp}(0)\\P_{III},O_{III},N_{III}:-V_{in}/2\end{cases}$	$\boldsymbol{C_{oss2}=2C_{oss2}}$, $\boldsymbol{R_L=4R_L}$, $\boldsymbol{C_{oss1}=2C_{oss1}}$ $V_s\begin{cases}P_{I\sim III}:NV_o/2\\O_{I\sim III}:Nv_{bs}(0)\\N_{I\sim III}:-NV_o/2\end{cases},V_p\begin{cases}P_I,O_I,N_I:V_{in}\\P_{II},O_{II},N_{II}:v_{bp}(0)\\P_{III},O_{III},N_{III}:0\end{cases}$

TABLE V
WORKING CONDITIONS FOR THE PROTOTYPE

Parameters	Range
Input voltage, V_{in}	50 V ~ 100 V
Switching frequency, f_s	50 kHz ~150 kHz
Load Resistor, R_L	30 Ω~ 400 Ω
Voltage gain, M	0.5 ~ 1.5
Output Power, P_o	20 W~ 200 W
Deadtime	170 ns

TABLE VI
KEY COMPONENTS FOR THE PROTOTYPE

Components	Parameters
MOSFET S_1~S_8	SCT3060AR
Resonant inductors L_{r1}, L_{r2}	PC95, PQ40/40, 10 turns
Transformer	PC95, PQ50/50
Litz wire	0.1 mm× 200
Transformer's turns number	10:10 for conditions 1~4 13:15 for conditions 5~12
Resonant capacitor	Metallized polypropylene film capacitors (MKP)

2) Different Operation Directions: The modeling process for different operation directions is similar. The only difference is the direction of parameters' conversion. When operating in backward direction, the circuit is converted to the secondary side, C_1 is equal to C_{r2}, L_1 is equal to L_{r2}, C_2 is equal to N^2C_{r1}, L_2 is equal to L_{r1}/N^2.

3) Different Structures of Inverters and Rectifiers: The former analysis is based on the full-bridge inverter and the full-bridge rectifier. However, when the structures of inverters and rectifiers change, some modifications are necessary. The detailed modifications are shown in Table IV.

IV. SIMULATION AND EXPERIMENTAL VERIFICATIONS

A. Verification of Waveforms

According to the operation mode analysis introduced in [11], [12], [13], [14], [15], [16], [17], and [18], there are four most widely used operation modes for *CLLLC* class resonant converters, which can be selected as the representative working conditions: 1) PO mode ($f_s < f_r$, normal load); 2) PN mode ($f_s < f_r$, heavy load); 3) OPO mode (light load); 4) NP mode ($f_s > f_r$, normal or heavy load). To cover these operation modes,

TABLE VII
LIST OF WORKING CONDITIONS

Working condition number	Resonant tank	L_{r1}/μH	L_{r2}/μH	C_{r1}/nF	C_{r2}/nF	L_m/μH	N	f_s/kHz	R_L/Ω	Operation mode in OMA	V_{in}/V
1	LLC	79.5	0	66.0	∞	195.9	1	55	100	PO	50
2									30	PN	70
3									400	OPO	
4								110	100	NP	
5	CLLC	94.8	0	58.6	53.0	208.3	13/15	70	100	PO	60
6									40	PN	
7									400	OPO	
8								110	100	NP	
9	ACLLLC	94.8	64.3	58.6	53.0	208.3	13/15	55	160	PO	60
10									80	PN	100
11									400	OPO	72
12								110	160	NP	80

a prototype as shown in Fig. 15 is established based on the working conditions shown in Table V. The key components are listed in Table VI. For resonant converters, some extra control methods such as the burst control are often applied for very light load conditions [33]. Therefore, around 10% load condition is considered for mode verification.

The main purpose of the experiment is conducted for the validation of model accuracy, instead of the high-performance design validation. Therefore, the parameters are designed using the traditional FHA based modeling and design method. Since there are many literatures about this design process [2], [3], [4], [5], [6], [7], [8], the detailed design process is not introduced in this article. The resonant tank parameters and selected working conditions are shown in Table VII. Additionally, the whole process of the proposed ASSA model can be applied for all kinds of MOSFET. In this work, the Silicon Carbide MOSFET SCT3060AR from Rohm is selected as a representative switching device for the validation process.

Fig. 16 shows the waveforms obtained by the proposed ASSA model, the traditional OMA model, and the experimental results. In order to verify the universality of the proposed model, the types of resonant tanks contain ACLLLC, *CLLC* and *LLC*. The analysis of the experimental waveforms and the ASSA calculated waveforms are listed as follows.

1) The phenomenon of the high frequency oscillation during O stage are theoretically analyzed in Section III-B, which can be depicted by ASSA and agrees well with the experimental results (marked with boxes in red dashed lines). Additionally, the duration of O stage will increase when converter works under light load [17], [18], [19], [20], which makes the high frequency oscillations longer and more obvious when operating under light load.
2) The resonant converter is always designed to works at the ZVS region. Therefore, the duration of II stage is short. However, compared with OMA, which ignores the II stage, the charging and discharging waveforms of the C_{oss1} (v_{S2}, green line waveforms) agree much better with the experimental results (marked with circles in blue dashed lines).
3) The errors of the proposed ASSA model and the OMA model compared with the experimental results are further depicted in Fig. 17. The maximum and minimum errors of OMA and ASSA methods are marked. The definition of the relative error is shown in (13), where $\|x\|_2$ means the two-norm value of the vector x. Fig. 17 shows that $Re(i_{Lr1})$, $Re(i_{Lr2})$ and the errors of i_{Lr1_rms}, i_{Lr1_peak}, I_{OFF}, $i_{Lr1,\ rms}$, $i_{Lr2,\ peak}$ are reduced significantly for most of the cases. Furthermore, $Re(i_{Lr1})$ and $Re(i_{Lr2})$ can be reduced from 5.91%–43.54% to 2.83%–19.42%, which means the AASA model depicts inductor current waveforms much more accurately

$$Re(i_{Lr}) = \frac{\|i_{Lr,model} - i_{Lr,experiment}\|_2}{\|i_{Lr,experiment}\|_2}. \tag{14}$$

Additionally, the selected deadtime is a constant value of 170 ns in the experimental test, which accounts for 0.935%–1.870% of one switching cycle (deadtime ratio). To further verify the universality of the ASSA model, the waveforms when deadtime ratio is varying from 0.5% to 15% are calculated by PSIM and the ASSA model. Fig. 18(a) and (b) shows the waveforms of i_{Lr1}, i_{Lr2}, which agree well with the PSIM results. The $Re(i_{Lr1})$ values for representative working conditions 1, 6, 11, 12 are shown in Fig. 18(c), small errors are achieved under different deadtime ratio.

This can be explained by the modeling process. The ASSA model considers all the possible switching status as different working stages. Therefore, the deadtime percentage has no effects on the switching status, working stages' possibilities and transition conditions, which means the flowchart in Fig. 12 has no changes with the variation of deadtime percentage.

B. Verification of Calculation Speed

The time domain model of resonant converters is often used for the iteration process in the parameter design optimization stage. Therefore, the fast calculation speed is required. This section verifies the fast calculation speed characteristic of the proposed hybrid OMA and SSA modeling method. For the traditional SSA model, the initial values $i_1(0)$, $i_2(0)$, $v_1(0)$, $v_2(0)$, and $V_o(0)$ are rarely discussed. If the initial values are set randomly or stat constant, there is a high probability that they are very far away from steady state values, which will highly increase

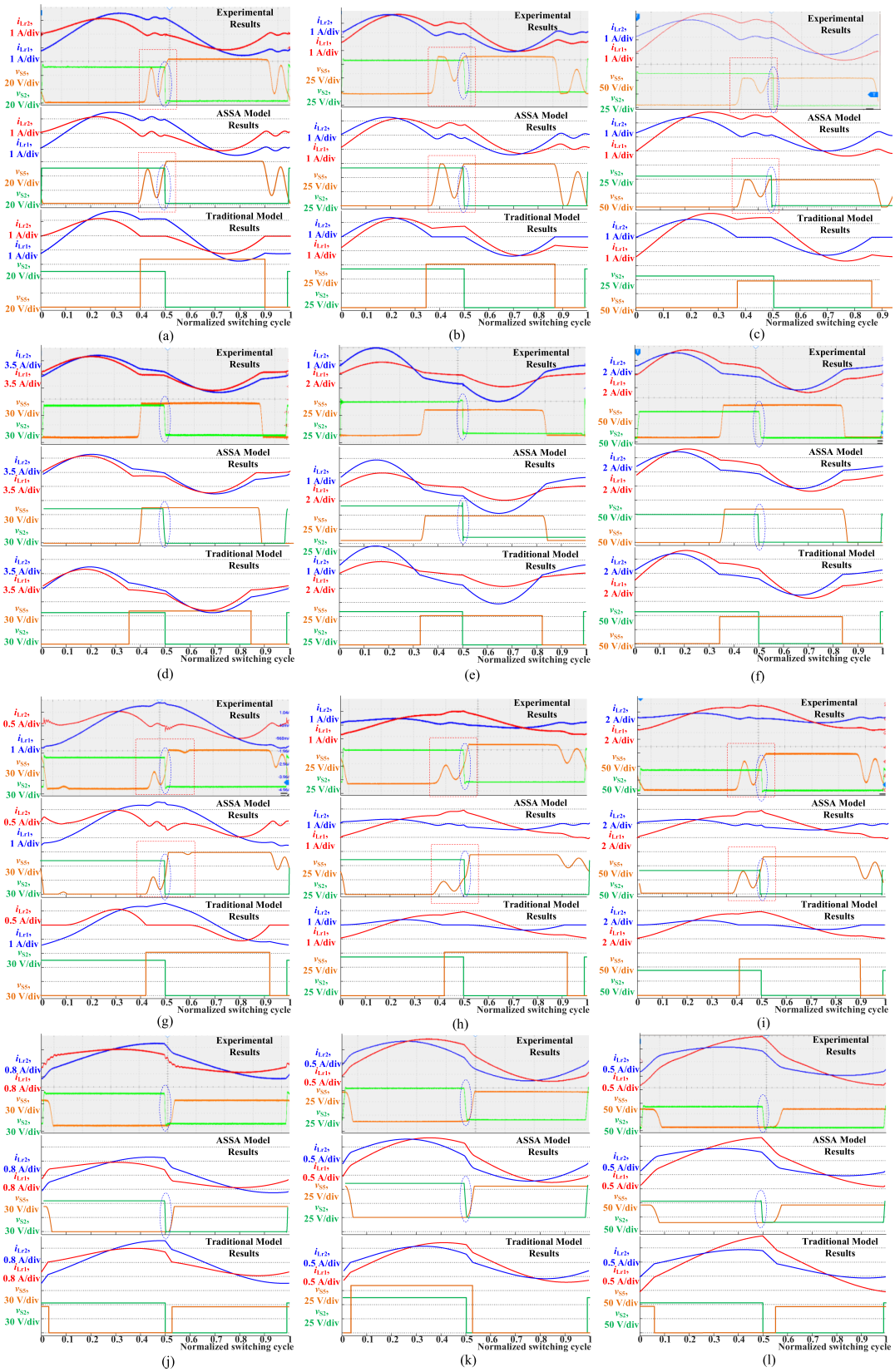

Fig. 16. Comparison among experimental results, ASSA model results and traditional model results for working conditions 1∼12. (a) Condition 1 (*LLC*, normal load, $f_s < f_r$). (b) Condition 5 (*CLLC*, normal load, $f_s < f_r$). (c) Condition 9 (ACLLLC, normal load, $f_s < f_r$). (d) Condition 2 (*LLC*, heavy load, $f_s < f_r$). (e) Condition 6 (*CLLC*, heavy load, $f_s < f_r$). (f) Condition 10 (ACLLLC, heavy load, $f_s < f_r$). (g) Condition 3 (*LLC*, light load, $f_s < f_r$). (h) Condition 7 (*CLLC*, light load, $f_s < f_r$). (i) Condition 11 (ACLLLC, light load, $f_s < f_r$). (j) Condition 4 (*LLC*, normal load, $f_s > f_r$). (k) Condition 8 (*CLLC*, normal load, $f_s > f_r$). (l) Condition 12 (ACLLLC, normal load, $f_s > f_r$).

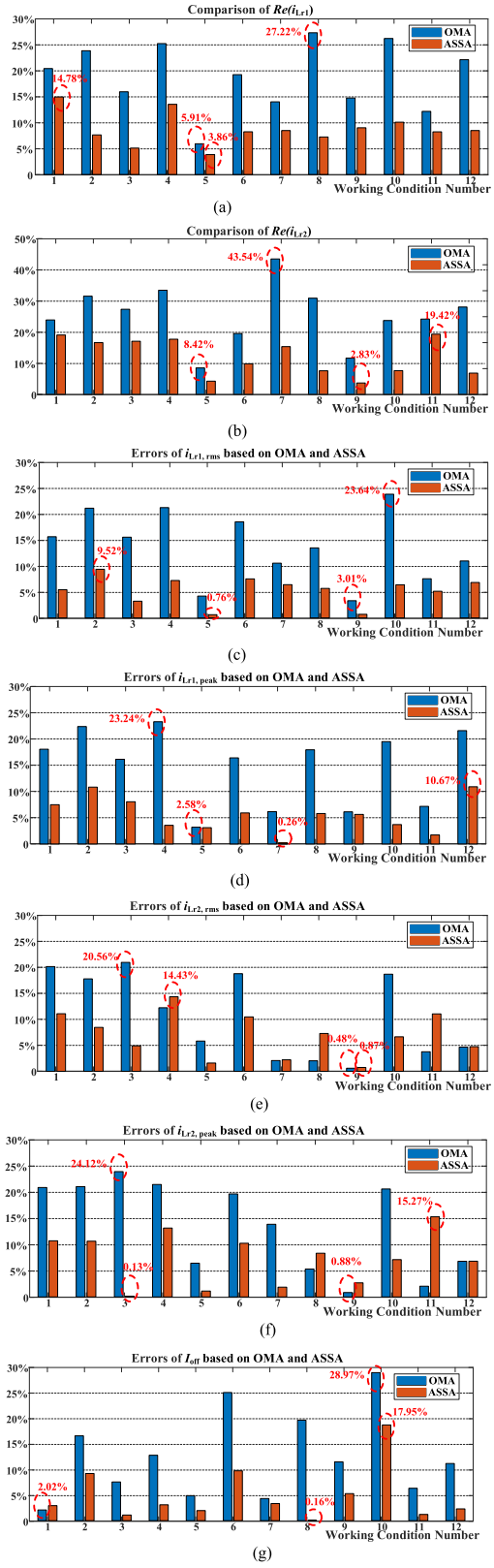

Fig. 17. Errors of the ASSA model and the traditional OMA model compared with the experimental results. (a) $Re(i_{\mathrm{Lr1}})$ of OMA and ASSA model. (b) $Re(i_{\mathrm{Lr2}})$ of OMA and ASSA model. (c) Errors of $i_{\mathrm{Lr1,\,rms}}$ based on OMA and ASSA model. (d) Errors of $i_{\mathrm{Lr1,\,peak}}$ based on OMA and ASSA model. (e) Errors of $i_{\mathrm{Lr,\,rms}}$ based on OMA and ASSA model. (f) Errors of $i_{\mathrm{Lr2,\,peak}}$ based on OMA and ASSA model. (g) Errors of I_{off} based on OMA and ASSA model.

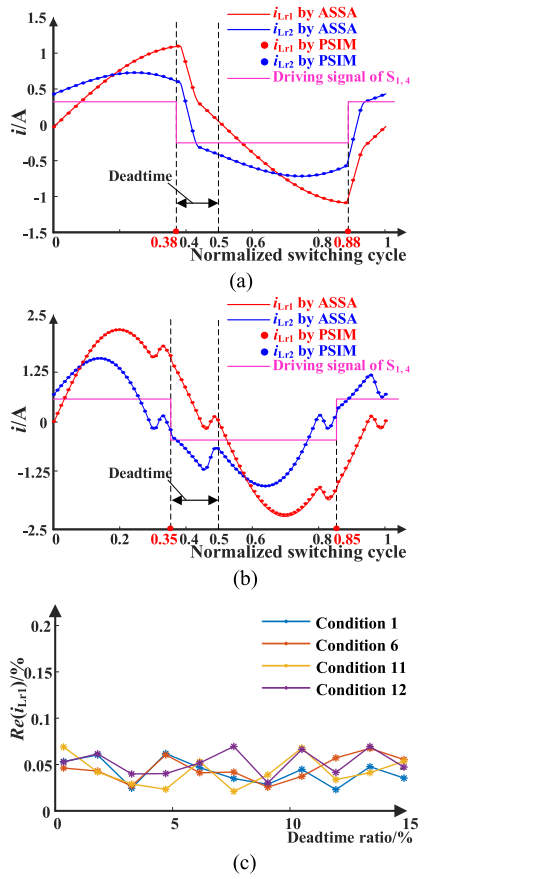

Fig. 18. Comparison of ASSA and PSIM results for different working conditions and deadtime ratio. (a) Condition 4, deadtime ratio is 12%. (b) Condition 1, deadtime ratio is 15%. (c) $Re(i_{\mathrm{Lr1}})$ for working conditions 1, 6, 11, 12 varying with the deadtime ratio.

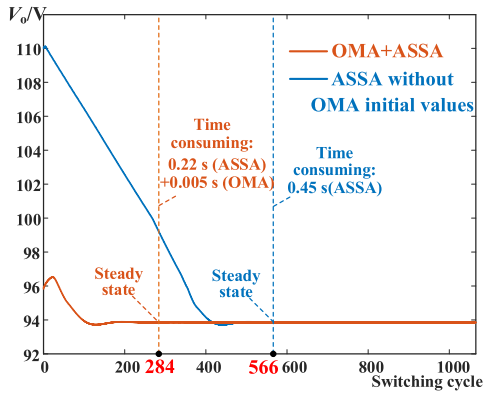

Fig. 19. Dynamic process of V_{O} using OMA initial values and far initial values in working condition 5.

the calculation time of the proposed ASSA model. Take the working condition 5 as an example, it can be seen in Fig. 19 that if the initial values are far away from steady state values, it takes 566 switching cycles to enter the steady state, the calculation time using MATLAB is 0.45 s. However, the OMA model has a much faster calculation speed (ms level using MATLAB), the calculation time consuming of OMA model can even be neglected. By using traditional OMA model to get the initial

TABLE VIII
COMPARISON OF CALCULATION TIME USING DIFFERENT MODELING METHODS AND SIMULATION TOOLS

Calculation/simulation condition	Step size	Average time consuming to get steady state waveforms in working conditions 1~12
PSIM	1 ns	53 s (279 units)
LTspice	Variable	>3600 s
Simulink	1 ns	478 s (2516 units)
PLECS	1 ns	49 s (258 units)
Constant initial values +ASSA	1 ns	0.41 s (2.15 units)
OMA+ASSA	1 ns	0.19 s (1 unit)

values, the initial values are not far from the steady state values. It can be seen from Fig. 18 that by using initial values obtained by OMA model, the ASSA model only takes 284 switching cycles to enter the steady state. The total time consuming of OMA+ASSA model is 0.225 s (ASSA: 0.22 s + OMA: 0.005 s). The further comparison of other working conditions is shown in Table VIII.

Additionally, the proposed ASSA model calculates the waveforms based on analytical expressions. Therefore, compared with the commercial simulation software, the calculation speed of ASSA model is much faster (279 times faster than PSIM). The comparison of the calculation speed is shown in Table VIII. The fast calculation speed of ASSA model makes it convenient to realize the optimal design of resonant tank parameters.

V. CONCLUSION

This article proposes an accurate, universal, and fast ASSA model for resonant converters. By considering the parasitic capacitors' charging and discharging process and primary side switches' reversely conduction process during deadtime, the newly introduced operation stages ($P_{I\sim III}$, $O_{I\sim III}$, $N_{I\sim III}$) are proposed and analyzed. To reduce the modeling complexity and improve the universality of ASSA, all different working stages are equivalent to one universal equivalent circuit, and can be applied to different resonant tanks, operation directions, and structures of inverter/rectifier by simply modifying the parameters. The experiment is conducted based on ACLLLC, *CLLC* and *LLC* resonant converters operating in different load conditions. By comparing the results of traditional OMA model, ASSA model and the experimental result, ASSA depicts waveforms much more accurately due to the consideration of more stages. $Re(i_{Lr1})$, $Re(i_{Lr2})$ and the errors of i_{Lr1_rms}, i_{Lr1_peak}, I_{OFF}, $i_{Lr1,\ rms}$, $i_{Lr2,\ peak}$ are compared. $Re(i_{Lr1})$ and $Re(i_{Lr2})$ can be reduced significantly from 5.91%–43.54% to 2.83%–19.42%. In addition, the calculation speed of the proposed hybrid OMA and SSA modeling method is much faster than commercial simulation tools (279 times faster than PSIM) and traditional constant initial values method (2.15 times faster).

REFERENCES

[1] Y. Wei, Q. Luo, and A. Mantooth, "Overview of modulation strategies for LLC resonant converter," *IEEE Trans. Power Electron.*, vol. 35, no. 10, pp. 10423–10443, Oct. 2020.

[2] J. Deng, S. Li, S. Hu, C. C. Mi, and R. Ma, "Design methodology of LLC resonant converters for electric vehicle battery chargers," *IEEE Trans. Veh. Technol.*, vol. 63, no. 4, pp. 1581–1592, May 2014.

[3] B. Yang, F. C. Lee, A. J. Zhang, and G. Huang, "LLC resonant converter for front end DC/DC conversion," in *Proc. 17th Annu. IEEE Appl. Power Electron. Conf. Expo.*, Dallas, TX, USA, 2002, vol. 2, pp. 1108–1112.

[4] J.-H. Jung, H.-S. Kim, M.-H. Ryu, and J.-W. Baek, "Design methodology of bidirectional CLLC resonant converter for high-frequency isolation of DC distribution systems," *IEEE Trans. Power Electron.*, vol. 28, no. 4, pp. 1741–1755, Apr. 2013.

[5] G. Ivensky, S. Bronshtein, and A. Abramovitz, "Approximate analysis of resonant LLC DC-DC converter," *IEEE Trans. Power Electron.*, vol. 26, no. 11, pp. 3274–3284, Nov. 2011.

[6] Z. U. Zahid, Z. M. Dalala, R. Chen, B. Chen, and J.-S. Lai, "Design of bidirectional DC–DC resonant converter for vehicle-to-grid (V2G) applications," *IEEE Trans. Transp. Electrific.*, vol. 1, no. 3, pp. 232–244, Oct. 2015.

[7] J. Min and M. Ordonez, "Bidirectional resonant CLLC charger for wide battery voltage range: Asymmetric parameters methodology," *IEEE Trans. Power Electron.*, vol. 36, no. 6, pp. 6662–6673, Jun. 2021.

[8] X. Li, J. Huang, Y. Ma, X. Wang, J. Yang, and X. Wu, "Unified modeling, analysis, and design of isolated bidirectional CLLC resonant DC–DC converters," *IEEE J. Emerg. Sel. Topics Power Electron.*, vol. 10, no. 2, pp. 2305–2318, Apr. 2022.

[9] J. Liu, J. Zhang, T. Q. Zheng, and J. Yang, "A modified gain model and the corresponding design method for an LLC resonant converter," *IEEE Trans. Power Electron.*, vol. 32, no. 9, pp. 6716–6727, Sep. 2017.

[10] A. Chandwani, A. Mallik, and A. Aktruk, "Parasitic component inclusive optimum phase-frequency contour enabled synchronous rectification of asymmetric CLLC resonant converter," *IEEE Open J. Power Electron.*, vol. 4, pp. 91–106, 2023.

[11] Y. Wei, Q. Luo, S. Chen, P. Sun, and N. Altin, "Comparison among different analysis methodologies for LLC resonant converter," *IET Power Electron.*, vol. 12, no. 9, pp. 2236–2244, Jul. 2019.

[12] X. Fang, H. Hu, Z. J. Shen, and I. Batarseh, "Operation mode analysis and peak gain approximation of the LLC resonant converter," *IEEE Trans. Power Electron.*, vol. 27, no. 4, pp. 1985–1995, Apr. 2012.

[13] R. Yu, G. K. Y. Ho, B. M. H. Pong, B. W.-K. Ling, and J. Lam, "Computer-aided design and optimization of high-efficiency LLC series resonant converter," *IEEE Trans. Power Electron.*, vol. 27, no. 7, pp. 3243–3256, Jul. 2012.

[14] J. F. Lazar and R. Martinelli, "Steady-state analysis of the LLC series resonant converter," in *Proc. 16th Annu. IEEE Appl. Power Electron. Conf. Expo.*, Anaheim, CA, USA, 2001, vol. 2, pp. 728–735.

[15] S. Ditze, "Steady-state analysis of the bidirectional CLLLC resonant converter in time domain," in *Proc. IEEE 36th Int. Telecommun. Energy Conf.*, Vancouver, BC, Canada, 2014, pp. 1–9.

[16] A. Kumar, A. Awasthi, O. Salari, S. Bagawade, and P. Jain, "A novel time domain analysis of the LLC-L resonant converter for the use of the CLL and LLC resonant converter," in *Proc. IEEE Appl. Power Electron. Conf. Expo.*, Anaheim, CA, USA, 2019, pp. 3453–3460.

[17] A. Kumar, A. Awasthi, O. Salari, A. Laha, and P. Jain, "An exact time-domain based novel simulation-design tool for study and optimal design of LLC and CLL resonant converters," in *Proc. IEEE Energy Convers. Congr. Expo.*, Baltimore, MD, USA, 2019, pp. 673–680.

[18] L. Wang, Q. Luo, and T. Luo, "A time-domain optimization design methodology for CLLC resonant converter," in *Proc. IEEE 1st Int. Power Electron. Appl. Symp.*, Shanghai, China, 2021, pp. 1–5.

[19] Y. Wei, Z. Wang, Q. Luo, and H. Alan Mantooth, "MATLAB GUI based steady state open-loop and closed-loop simulation tools for different LLC converters with all operation modes," *IEEE Open J. Ind. Appl.*, vol. 2, pp. 320–336, 2021.

[20] L. Zhao, Y. Pei, L. Wang, L. Pei, W. Cao, and Y. Gan, "Design methodology of bidirectional resonant CLLC charger for wide voltage range based on parameter equivalent and time domain model," *IEEE Trans. Power Electron.*, vol. 37, no. 10, pp. 12041–12064, Oct. 2022.

[21] J. Sun, L. Yuan, Q. Gu, R. Duan, Z. Lu, and Z. Zhao, "Design-oriented comprehensive time-domain model for CLLC class isolated bidirectional DC-DC converter for various operation modes," *IEEE Trans. Power Electron.*, vol. 35, no. 4, pp. 3491–3505, Apr. 2020.

[22] B. Xue, L. Wang, M. Fu, and H. Wang, "State-space based universal time-domain model for voltage-fed bidirectional IPT systems," *IEEE Trans. Ind. Electron.*, vol. 71, no. 1, pp. 615–624, Jan. 2024.

[23] T. Luo et al., "A full-iteration optimal design methodology of CLLC converter with minimized RMS current," *IEEE Trans. Power Electron.*, vol. 39, no. 10, pp. 11916–11930, Oct. 2024.

[24] S. Zhang, Y. Wei, and J. Liu, "A dynamic time-domain based accurate small signal model for LLC converter," in *Proc. IEEE 14th Int. Symp. Power Electron. Distrib. Gener. Syst.*, Shanghai, China, 2023, pp. 984–989.

[25] L. Yuan et al., "A comprehensive design-oriented time-domain model for isolated bidirectional DC-DC converter considering dead-time effect," in *Proc. 23rd Int. Conf. Elect. Machines Syst.*, Hamamatsu, Japan, 2020, pp. 1046–1051.
[26] S. Ditze, T. Heckel, and M. März, "Influence of the junction capacitance of the secondary rectifier diodes on output characteristics in multi-resonant converters," in *Proc. IEEE Appl. Power Electron. Conf. Expo.*, Long Beach, CA, USA, 2016, pp. 864–871.
[27] Z. Xiao, Z. He, R. Guan, and A. Luo, "Piecewise-approximated time domain analysis of LLC resonant converter considering parasitic capacitors and deadtime," *IEEE Trans. Power Electron.*, vol. 38, no. 1, pp. 578–592, Jan. 2023.
[28] H. Chen, L. Wang, K. Sun, and L. Lu, "A switching delay strategy for sensorless synchronous rectification in CLLC converters," *IEEE Trans. Power Electron.*, vol. 39, no. 1, pp. 280–293, Jan. 2024.
[29] M. Kasper, R. M. Burkart, G. Deboy, and J. W. Kolar, "ZVS of power MOSFETs revisited," *IEEE Trans. Power Electron.*, vol. 31, no. 12, pp. 8063–8067, Dec. 2016.
[30] K. Wang, X. Yang, L. Wang, and P. Jain, "Instability analysis and oscillation suppression of enhancement-mode GaN devices in half-bridge circuits," *IEEE Trans. Power Electron.*, vol. 33, no. 2, pp. 1585–1596, Feb. 2018.
[31] D. Costinett, D. Maksimovic, and R. Zane, "Circuit-oriented treatment of nonlinear capacitances in switched-mode power supplies," *IEEE Trans. Power Electron.*, vol. 30, no. 2, pp. 985–995, Feb. 2015.
[32] N. Wang, H. Jia, M. Tian, Z. W. Li, G. Z. Xu, and X. Yang, "Impact of transformer stray capacitance on the conduction loss in a GaN-based LLC resonant converter," in *Proc. IEEE 3rd Int. Future Energy Electron. Conf. ECCE Asia*, Kaohsiung, Taiwan, 2017, pp. 1334–1338.
[33] W. Feng, F. C. Lee, and P. Mattavelli, "Optimal trajectory control of burst mode for LLC resonant converter," *IEEE Trans. Power Electron.*, vol. 28, no. 1, pp. 457–466, Jan. 2013.
[34] H. Liu, L. He, Q. Sun, and C. Men, "Design and simulation of a PFM-PWM hybrid controller for DCDC converter with CLLC topology," in *Proc. China Semicond. Technol. Int. Conf.*, Shanghai, China, 2023, pp. 1–3.
[35] S. Esmailirad, R. Beiranvand, and A. Y. Varjani, "Using the frequency and pulse width modulation techniques for regulating the LLC resonant converter output voltage," in *Proc. 9th Annu. Power Electron., Drives Syst. Technol. Conf.*, Tehran, Iran, 2018, pp. 30–37.
[36] Z. Xiao, Z. Li, Z. He, H. Wang, Y. Tang, and A. Luo, "Computer-aided time-domain operation and design optimization of resonant converters," *IEEE J. Emerg. Sel. Topics Power Electron.*, vol. 11, no. 4, pp. 4164–4177, Aug. 2023.

Ziang Li (Student Member, IEEE) received the B.S. degree in electrical engineering from Xi'an Jiaotong University, Shaanxi, China, in 2022. He is currently working toward the Ph.D. degree with Xi'an Jiaotong University, Shaanxi, China. His current working subject is accurate model, optimal design of DC–DC converters.

His current research interests include modeling, trajectory control, and design methodology of resonant converters.

Shuo Zhang (Student Member, IEEE) received the B.S. degree in electrical engineering from Tianjin University, Tianjin, China, in 2023. He is currently working toward the Ph.D. degree with Xi'an Jiaotong University, Xi'an, China.

His current research interests include modeling, control, and optimal design of resonant converters.

Dachuan Chen received the B.S. degree in electrical engineering and automation from North China Electric Power University, Baoding, China, in 2018, and the Ph.D. degree in electrical engineering from Shanghai Jiao Tong University, Shanghai, China, in 2023.

His research interests include dc–dc converters, inductors, and high-frequency losses.

Peng Sun was born in Jilin province, China, in 1994. He received the bachelor's and Ph.D. degrees in electrical engineering from North China Electric Power University, Beijing, China, in 2016 and 2022, respectively.

He was a visiting scholar with the University of Arkansas, Fayetteville, AR, USA, from 2019 to 2020. He is currently a Lecture with the State Key Laboratory of Alternate Electrical Power System with Renewable Energy Sources, North China Electric Power University. His research interests include the packaging, condition monitoring, and reliability of power electronics devices.

Yanjie He (Student Member, IEEE) received the B.S. degree in electrical engineering from Xi'an Jiaotong University, Xi'an, China, in 2023. He is currently working toward the M.S. degree in electrical engineering with Xi'an Jiaotong University, Xi'an, China, and with Politecnico di Milano, Milan, Italy.

His research interests include the modeling of wide bandgap devices and its applications.

Quanming Luo (Member, IEEE) was born in Chongqing, China, in 1976. He received the B.S., M.S., and Ph.D. degrees in electrical engineering from the Chongqing University, Chongqing, China, in 1999, 2002, and 2008, respectively.

Since 2005, he has been with the college of Electrical Engineering, Chongqing University, where he is currently a Professor. He has authored or coauthored more than 80 papers in journal or conference proceedings. His current research interests include LED driving systems, communication power systems, power harmonic suppression, and power conversion systems in electrical vehicles.

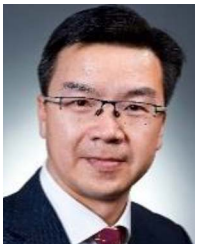

Jinjun Liu (Fellow, IEEE) received the B.S. and Ph.D. degrees in electrical engineering from Xi'an Jiaotong University (XJTU), Xi'an, China, in 1992 and 1997, respectively.

He was a faculty with the Electrical Engineering School, XJTU. From late 1999 to early 2002, he was with the Center for Power Electronics Systems, Virginia Polytechnic Institute and State University, Blacksburg, VA, USA, as a Visiting Scholar. In late 2002, he was promoted to a Full Professor and then the Head of the Power Electronics and Renewable Energy Center, XJTU, which currently comprises more than 20 faculty members and more than 200 graduate students and carries one of the leading power electronics programs in China. From 2005 to early 2010, he was an Associate Dean with the Electrical Engineering School, XJTU, and from 2009 to early 2015, the Dean for Undergraduate Education of XJTU. He is currently a XJTU Distinguished Professor of Power Electronics. He coauthored 3 books (including one textbook), published more than 500 technical papers in peer-reviewed journals and conference proceedings, holds more than 70 invention patents (China/US/EU), and delivered for many times plenary keynote speeches and tutorials at IEEE conferences or China national conferences. His research interests include modeling, control, and design methods for power converters and electronified power systems, power quality control and utility applications of power electronics, and microgrids for sustainable energy and distributed generation.

Dr. Liu was the recipient of many times governmental awards at national level or provincial/ministerial level for scientific research/teaching achievements. He is also the recipient of the 2006 Delta Scholar Award, the 2014 Chang Jiang Scholar Award, the 2014 Outstanding Sci-Tech Worker of the Nation Award, the 2016 State Council Special Subsidy Award, IEEE TRANSACTIONS ON POWER ELECTRONICS 2016 and 2021 Prize Paper Awards, the Nomination Award for the Grand Prize of 2020 Bao Steel Outstanding Teacher Award, and the 2022 Fok Ying Tung Education and Teaching Award. He was the IEEE Power Electronics Society Region 10 Liaison and then China Liaison for 10 years, has been an Associate Editor for IEEE TRANSACTIONS ON POWER ELECTRONICS since 2006, 2015–2019 Executive Vice President and 2020 and 2021 Vice President of IEEE Power Electronics Society. He was on the Board of China Electrotechnical Society 2012–2020 and was elected the Vice President in 2013 and the Secretary General in 2018 of the CES Power Electronics Society. He was 2013–2021 Vice President for International Affairs, China Power Supply Society (CPSS), and since 2016, has been the inaugural Editor-in-Chief of *CPSS Transactions on Power Electronics and Applications*. He was elected the President of CPSS in Nov. 2021. Since 2013, he has been the Vice Chair of the Chinese National Steering Committee for College Electric Power Engineering Programs.

Yuqi Wei (Member, IEEE) was born in Henan, China, in 1995. He received the B.S. degree from Yanshan University, Hebei, China, in 2016, the M.S. degree from the University of Wisconsin-Milwaukee (UWM), Milwaukee, WI, USA, in 2018, the M.S. degree from Chongqing University, Chongqing, China, in 2019, and the Ph.D. degree from the University of Arkansas, Fayetteville, AR, USA, in 2022, all in electrical engineering.

He was a Visiting Researcher with Kiel University, Germany from Sep. to Dec. 2021. He was a Postdoc Researcher with the University of Arkansas in 2022. Since 2023, he has been a tenure track Research Professor with Xi'an Jiaotong University. His current research interests include wide band gap devices, design automation, and cryogenic power electronics.

Dr. Wei was the recipient of the 2020 IEEE Power Electronics Society Transactions Second Place Prize Paper Award, 2021 IEEE International Future Energy Electronics Conference best conference paper award, 2022 IEEE Transportation Electrification Council Prize Ph.D. Thesis Talk Award, and 2022 IEEE Energy Conversion Congress and Exposition prize paper award.